J. Webster (ed.), *Wiley Encyclopedia of Electrical and Electronics Engineering*


# HOLOGRAPHIC STORAGE

Holographic data storage systems store 2-D data patterns in the form of holograms. The use of thick media allows multiplexing of a large number of holograms in the same media volume, and the number of multiplexed holograms can be as high as a few percent of the thickness-to-wavelength ratio, media permitting. Therefore, holographic storage offers two very attractive features: high data capacity and high data transfer rate. The latter property is a result of the nature of parallel readout of the 2-D data pattern. For a recent review, see Refs. 1,2,3,4,5,6.

Figure 1 shows a generic holographic storage system. During recording, electronic data are loaded into the optical spatial modulator (*SLM*), which spatially modulates the signal beam. The signal beam, upon interfering with a reference beam inside the recording media, forms a complex interference pattern that is replicated in the media as a refractive index pattern. During readout, the media are illuminated with a reference beam, identical to the one used in the recording, causing the complex grating to diffract a fraction of the reference beam to re-create the stored image. The detector (e.g., a charge coupled device, *CCD*) captures this image and converts it back to electronic data. A number of pages can be multiplexed in the same media volume provided they are recorded with reference beams having different wave vectors. Because of the Bragg selectivity property of thick holograms, each page can be recalled independently by a reference beam whose wave vector matches the write reference wave vector.

As shown in Fig. 1, the modulated beam is normally focused (i.e., Fourier transformed) by the Fourier transform lens (*FTL*) onto the recording media to minimize the spatial extent of the data. The reference beam is passed through a multiplexer, which directs the reference beam to land at the recording site at selected angles. Upon readout, the diffracted signal from the media is inverse Fourier transformed by the inverse Fourier transform lens (*IFTL*) and captured by CCD. Not shown in Fig. 2 are the optical modulators that switch the beams on and off during the operation and the polarization rotators that control the beam polarizations.

Holographic storage with 2-D media was actively researched in the early 1960s (7–12) but became dormant because early efforts were hampered by immature component technologies. Additionally, it was not as attractive as bit serial storage in density. Recent advances in 3-D storage media and in lasers, SLM, and CCD have caused a renewed interest in holographic storage. At the present time, the major difficulty still lies in the lack of a mature enough 3-D holographic storage medium.

## Purpose and Methodology

The bottom line parameters of importance for holographic storage are the density $D$ and the transfer rate $\nu_r$. Here, $\nu_r$ represents the read transfer rate. The write transfer rate is also important but has a more complicated dependence on media properties such as sensitivity and reciprocity; it will not be addressed in this paper. Under the constraint of a given *SNR* requirement of the overall system, it can be shown that when we increase $\nu_r$, then the diffraction efficiency $\eta$ must be larger, which will then lead to a lower storage density for media with a finite dynamic range $\Delta n$, or vice versa. However, the trade-off is not a linear one.

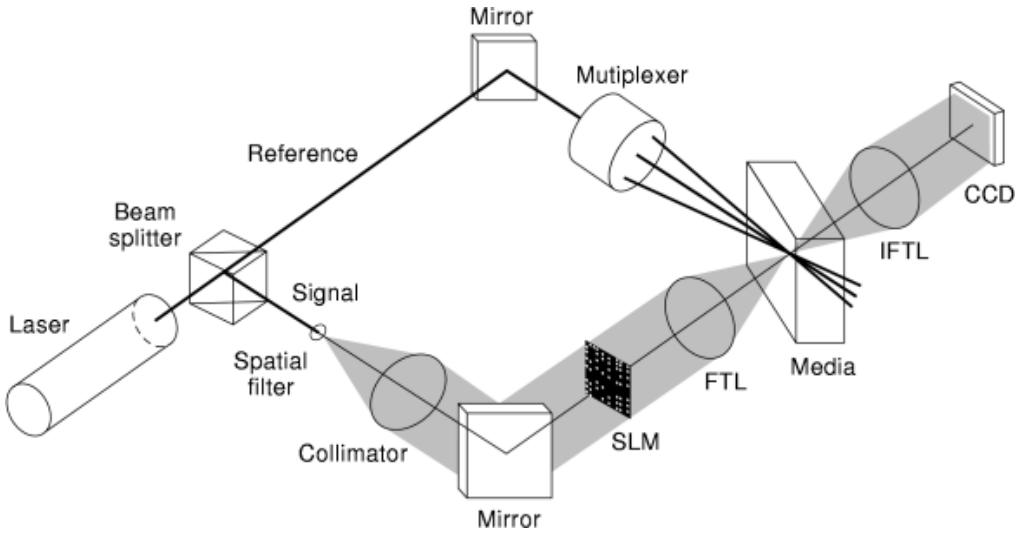


**Fig. 1.** Diagram of a holographic storage that employs angular multiplexing. The essential building blocks of the optical architecture are all contained in this diagram.

The purpose of this article is to quantify the preceding statement with detailed analysis, in the context of a thick medium with a given media noise index $\chi$ and dynamic range $\Delta n$. This will provide the starting design framework of a holographic storage system, where the trade-off between the media and the system can be clearly addressed.

This article will focus on the angle multiplexing architecture where the reference beam and the signal beam are incident on the same media surface. We will not address another type of architecture where the two beams are incident on two different media surfaces with the $0^\circ/90^\circ$ geometry (1,13). The latter has somewhat different trade-off rules and promises higher volume storage densities. Even though it is quite straightforward to employ large storage space in the form of say a disk for the former architecture, it is difficult to extend from a single piece of cube to a large volumetric space effectively with the latter architecture.

Our analysis methodology is described in the flow diagram shown in Fig. 2. We first establish the equations for the storage density $D$ in terms of the number of pages per stack and the area occupied by the stack. By stack, we mean the area occupied by the multiplexed holograms in the same volumetric space. The number of pages per stack $N_{\mathrm{pg}}$ is limited by the dynamic range $\Delta n$ and the diffraction efficiency per hologram $\eta$. The area occupied by each stack is a complicated function of $\lambda$, F_number of the Fourier optics, media thickness $d$, and $N_{\mathrm{SLM}}$, the number of pixels per side for the SLM and the recording geometry. The results of the trade-off studies between $D$ and the material and optics parameters will be given in the section entitled "Storage Density Limits." We then establish the equations for the transfer rate $\nu_{\mathrm{r}}$ as constrained by the interpage cross-talk $\mathrm{SNR}_{\mathrm{pg}}$, the media noise index $\chi$ (to be defined in the subsection entitled "Noise"), and $\eta$, which determines the amount of signal photons falling on the CCD. The trade-off between $\nu_{\mathrm{r}}$ and the different noise contributions and $\eta$ will be given in the section entitled "Read Transfer Rate."

Since the common parameter for $D$ and $\nu_{\mathrm{r}}$ is $\eta$, this allows us to establish the trade-off relation between the storage density and the transfer rate clearly. We will present the relation in closed form in the section entitled "Trade-off Between the Storage Density and the Transfer Rate." Furthermore, we established the trade-off between the dynamic range $\Delta n$ and the noise index $\chi$ in order to achieve the highest possible storage density for holographic storage.

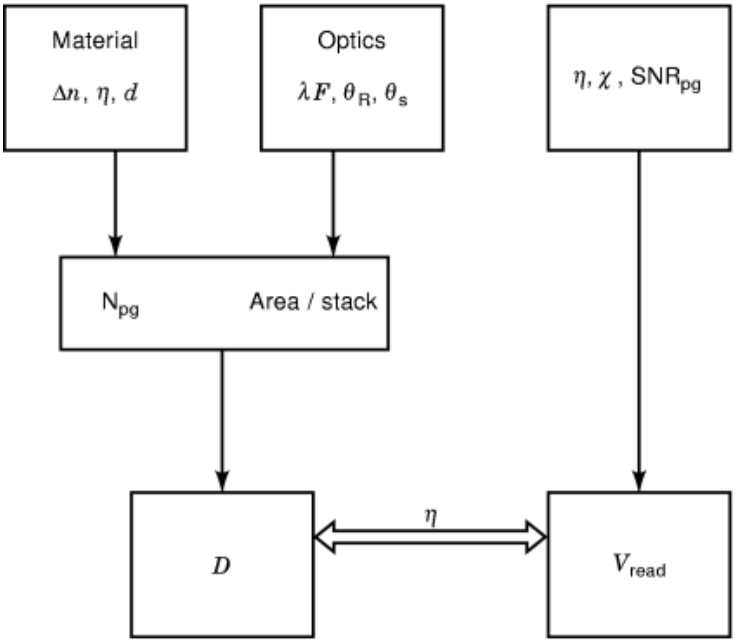


**Fig. 2.** Flow diagram of trade-off analysis between storage density and the data transfer rate. The blocks on the left side derive the dependence of the storage density on the material parameters and the optical parameters, while the two blocks on the right derive the dependence of the transfer rate on the diffraction efficiency and the signal-to-noise. The storage density and the transfer rate are tied together via the diffraction efficiency.

## Principles of Thick Holograms

**Review of the Theory of Thick Holograms.** The foundation of thick hologram theory was laid in Kogelnik's 1969 paper (14) using coupled mode equations. Consider a uniform phase grating inside a media of thickness $d$ (see Fig. 3), with a space-dependent refractive index,

$$n_{\text{tot}}(\boldsymbol{r}) = n + \Delta n \cos(\boldsymbol{K} \cdot \boldsymbol{r}) \tag{1}$$

where $n$ is the average refractive index, $\Delta n$ is the magnitude of the refractive index modulation, and $\boldsymbol{K}$ is the grating vector. The grating vector $\boldsymbol{K}$ has a magnitude

$$|\boldsymbol{K}| = K = \frac{2\pi}{\Lambda} \tag{2}$$

and a direction making an angle $\phi$ with respect to the $z$ axis.

Using the wave equation

$$\nabla^2 E(\boldsymbol{r}) + k^2 n(\boldsymbol{r})^2 E(\boldsymbol{r}) = 0 \tag{3}$$

we look for a diffraction solution of the form

$$E(x,z) = R(z)e^{j\mathbf{k}_R \cdot \mathbf{r}} + S(z)e^{j\mathbf{k}_S \cdot \mathbf{r}} \tag{4}$$

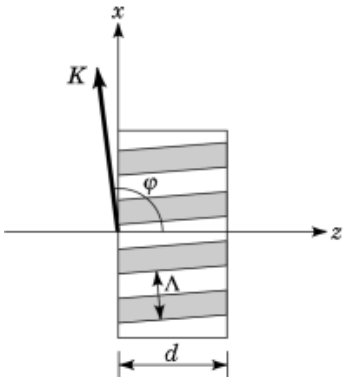


**Fig. 3.** Geometry of a thick hologram grating.

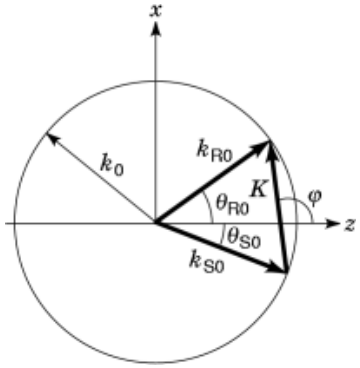


**Fig. 4.** Vector diagram of Bragg condition is the foundation of thick holograms.

where the reference beam with an amplitude of $R(z)$ and wave vector $\boldsymbol{k}_{\mathrm{R}}$ is incident on the grating causing a diffraction with amplitude of $S(z)$ and vector $\boldsymbol{k}_{\mathrm{S}}$. Also, $R(0) = 1$ and $S(z \leq 0) = 0$. This solution can be found from first-order perturbation near the Bragg condition. The Bragg condition (identified by subscripts 0) is expressed as

$$\boldsymbol{K} = \boldsymbol{k}_{\mathrm{R0}} - \boldsymbol{k}_{\mathrm{S0}} \tag{5}$$

This situation is described by the vector diagram in Fig. 4, which is conveniently drawn on a circle of radius $k_0 = 2\pi n_0/\lambda$. $\theta_{\mathrm{R0}}$ and $\theta_{\mathrm{S0}}$ are the angle that $\boldsymbol{k}_{\mathrm{R0}}$ and $\boldsymbol{k}_{\mathrm{S0}}$ make with the $z$ axis, respectively. $\lambda$ is the free space wavelength.

Varying of $\boldsymbol{k}_{\mathrm{R0}}$ by $\delta\theta$ in direction and $\delta\lambda$ in wavelength and inserting Eq. (4) into Eq. (3), Kogelnik found that the first-order perturbation solution is

$$S(d) = i\sqrt{\frac{c_{\mathrm{R}}}{c_{\mathrm{S}}}}\, e^{-i\xi} \frac{\sin(\sqrt{\xi^2 + \nu^2})}{\sqrt{1 + \xi^2/\nu^2}} \tag{6}$$

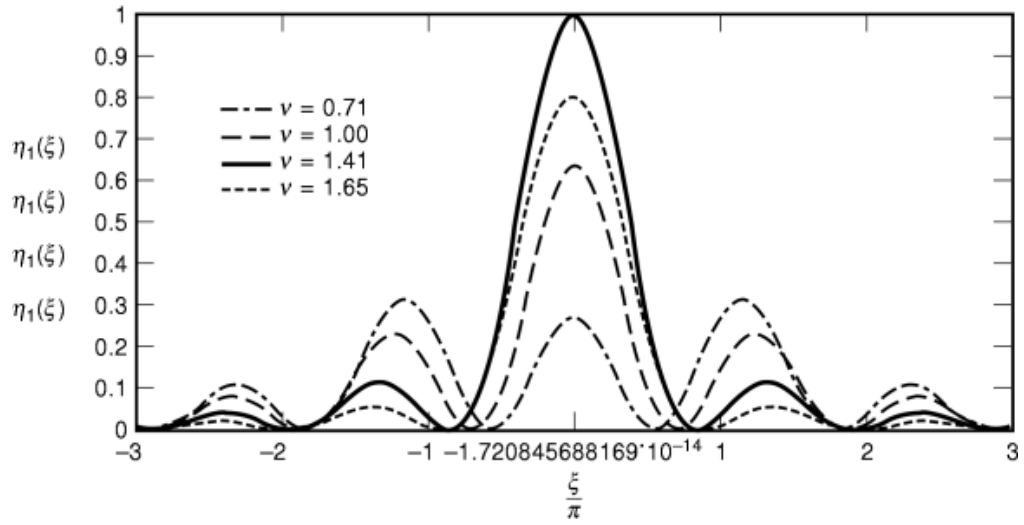


**Fig. 5.** $\eta$ versus $\xi$ for various values of $\nu$. It shows that the diffracted intensities are dependent on the degree of refractive index modulation, and it also shows the existence of the side lobes, which would cause cross-talk amongst adjacent holograms.

where $\xi$ is the Bragg mismatch parameter,

$$\xi = \frac{Kd}{2c_S}\sin(\varphi - \theta_R)\delta\theta - \frac{K^2 d}{8\pi n_0 c_S}\delta\lambda \tag{7}$$

(a third term, $\delta n$, can be added to include the possibility of controlling the Bragg condition through variation of the bulk refractive index in electrooptic materials by electric field), and the modulation parameter $\nu$ is

$$\nu = \frac{\pi \Delta n d}{\lambda\sqrt{c_R c_S}} \tag{8}$$

The geometry factors $c_R$ and $c_S$ are

$$c_R = \cos\theta_R, \quad c_S = c_R - K\cos\varphi/k \tag{9}$$

The second part of Eq. (9) states that the signal is diffracted at an angle $\theta_S = \cos^{-1}[\cos\theta_R - K\cos\phi/k_0]$. The diffraction efficiency $\eta$ is

$$\eta \equiv \frac{c_S|S(d)|^2}{c_R|R(0)|^2} = \frac{\sin^2(\sqrt{\xi^2+\nu^2})}{1+\xi^2/\nu^2} \tag{10}$$

The dependency of $\eta$ on $\xi$ and $\nu$ is shown in Fig. 5.

For small a modulation, $\eta$ approaches a $\text{sinc}^2$-function of $\xi$:

$$\eta = \nu^2 \frac{\sin^2 \xi}{\xi^2} \tag{11}$$

In the presence of uniform absorption, Eq. (10) must be replaced by

$$\eta = e^{-\alpha d} \frac{\sin^2(\sqrt{\xi^2 + \nu^2})}{1 + \xi^2/\nu^2} \tag{12}$$

where $\alpha$ is the absorption constant. Also for notation simplicity, we will drop 0 from quantities at the Bragg condition.

In holographic storage, the read reference wave vector is taken to be the same as the write reference wave vector for a single $\lambda$ system. This is not only a practical matter, but necessary. The object beam usually contains multiple wave vectors (Fourier transform of the data image); therefore, simultaneous satisfaction of Bragg condition for all wave vectors can happen only when the read and write reference wave vectors are either identical or antiparallel.

**Multiplexing.**

*Principles.* Multiplexing is based on two properties: Bragg selectivity and Bragg degeneracy.

*Selectivity.* We have seen that a sufficiently large deviation from Bragg condition, expressed by the Bragg mismatch parameter

$$\xi = \frac{Kd}{2c_S} \sin(\varphi - \theta_R)\delta\theta - \frac{K^2 d}{8\pi n_0 c_S} \delta\lambda \tag{13}$$

will result in little reconstruction of the diffracted signal. And the thicker the media, the higher the selectivity will be.

Let us consider angle multiplexing at a fixed wavelength ($\delta\lambda = 0$). To multiplex as many pages as possible in a given $\theta$ range, a small value of $\xi$ is desirable. However, it is obvious that small $\xi$ can potentially give rise to large interpage cross-talk. For small refractive index modulation, usually the case in holographic storage, the $\text{sinc}^2$ form of the diffracted signal suggests that two consecutive pages should be separated by

$$\xi_\alpha = \alpha\pi, \quad \alpha = 1, 2, \ldots \tag{14}$$

to minimize cross-talk. $\alpha$ is referred as page-separation parameter. Under the condition in Eq. (14), the peak of a given page coincides with the $\alpha$th zeros of its immediate neighbors. For complex gratings (as opposed to uniform planar gratings), the angular profile minima are not exactly zero. As will be shown in the subsection entitled "Noise," higher and noninteger $\alpha$ values will be needed to reduce the cross-talk at the price of reducing the number of pages that can be multiplexed.

*Degeneracy.* A pair of writing beams produces a unique grating. The converse is, however, not true. There are infinitely many possible reference beams with different incident angles and/or wavelengths that satisfy the Bragg condition in Eq. (2), [i.e., making an angle $\cos^{-1}(K/2k)$ with the grating vector] and, therefore, reconstruct the hologram. The loci of all wave vectors that recall a given grating vector $\boldsymbol{K}$ form a family of two-sided cones, as illustrated in Fig. 6.

Therefore, multiplexing is a systematic method to organize a number of grating vectors so that they are separated from each other by the selectivity and are not degenerately reconstructed (are not lying in the

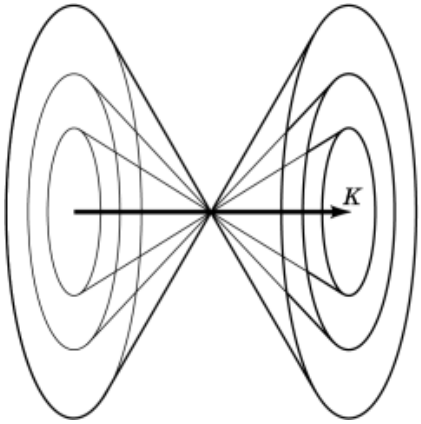


**Fig. 6.** Degeneracy of hologram readout. That is, there are many different reference beam vectors that can retrieve the same hologram.

intersection of two or more cones). A number of multiplexing methods are known. They are all based on the clever exploitation of the selectivity and degeneracy properties. The most common method is angle multiplexing. Angle multiplexing has been used since the early days of holographic storage (7,8,9,10,11,12) and is still widely employed (1,2,3,4,5,6,15,16,17). Other multiplexing methods have been proposed over the years: wavelength multiplexing (7,18), peristhropic multiplexing (19,20), shift multiplexing (21,22,23), and phase multiplexing (24,25,26,27,28,29,30). For the rest of the discussion, we will confine ourselves to angle multiplexing at a fixed wavelength ($\delta\lambda = 0$).

*Angle Multiplexing.* In angle multiplexing, $\xi$ is controlled by varying the angle between the reference wave vector $\boldsymbol{k}$ and the grating vector $\boldsymbol{K}$ at a fixed wavelength. To leave the Bragg cones as fast as possible, the angle variation must lie in the $\boldsymbol{k}$–$\boldsymbol{K}$ plane. This is equivalent to the requirement that all the reference and the signal beams must be in the reference-signal plane. Angle multiplexing can be accomplished by either changing the reference incident angle or rotating the media (around an axis normal to the reference-signal plane). The latter, however, introduces abberations and is not commonly adopted in practical implementations. Therefore, we will consider only the case where the reference incident angle is varied. The vector diagram is shown in Fig. 7.

Applying the "$\alpha\pi$-separation" criteria of Eq. (14) in Eq. (13), the angular change between two consecutive pages is

$$\delta\theta_{\alpha\pi} = \frac{\alpha\lambda\cos\theta_{\mathrm{S}}}{n_0 d\sin(\theta_{\mathrm{R}} + \theta_{\mathrm{S}})} \tag{15}$$

where $\theta_{\mathrm{R}}$ and $\theta_{\mathrm{S}}$ are the reference and signal incident angles inside the media. Integrating over the available reference angle range, $\theta_{\mathrm{R,min}} \le \theta_{\mathrm{R}} \le \theta_{\mathrm{R,max}}$, we obtain the number of multiplexed pages $N_{\mathrm{pg}}$ in a stack:

$$N_{\mathrm{pg}} = \int_{\theta_{\mathrm{R,min}}}^{\theta_{\mathrm{R,max}}} \frac{d\theta_{\mathrm{R}}}{\delta\theta_{\alpha\pi}} = \frac{\mu_{\mathrm{MX}}\, nd}{\alpha\lambda} \tag{16}$$

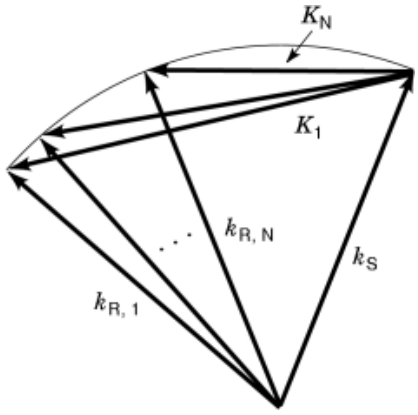


**Fig. 7.** Vector diagram for angle multiplexing. It shows how the different holographic grating vectors are generated by different reference beam vectors.

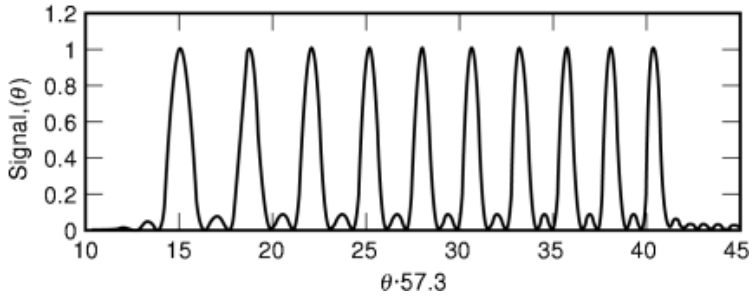


**Fig. 8.** Ten angularly multiplexed holograms with $3\pi$ separation.

where $\mu_{MX}$ is given by

$$\mu_{MX} \equiv \frac{\cos(\theta_{R,\min} + \theta_S) - \cos(\theta_{R,\max} + \theta_S)}{\cos\theta_S} \qquad (17)$$

For the purpose of illustration, we show the angle multiplexing of ten pages with $\alpha = 3$ in Fig. 8. The parameters used are $\lambda = 0.5$ $\mu$m, $n = 1.5$, $d = 30$ $\mu$m, $\alpha = 3$, and $\theta_S = 15^\circ$. The reference angular range is from $\theta_R = 15.0^\circ$ to $40.4^\circ$ (which corresponds to an external angular range of $\Theta_R = 23^\circ$ to $76^\circ$).

**Noise.** The presence of noise introduces limitations to holographic storage system performance. High noise must be compensated by a large signal to yield good data recovery, but at the price of consuming the dynamic range and hence reducing storage density. Therefore, it is necessary to quantify noise in details. In this section, we will discuss three types of noise that arise in holographic storage: media scatter noise, interpage cross-talk noise, and detector noise.

*Media Scatter Noise.* Illumination of the media during readout produces the desired signal along with scatter lights whose spatial distribution depends on the media optical properties. The scatter noise distribution is described by $B(\Theta, \Phi)$—the scatter noise power in the direction $(\Theta, \Phi)$ per unit incident power per unit solid angle, where $\Theta$ and $\Phi$ are the polar and azimuthal angles, respectively. If the scatter source is d'Lambertian,

then $B$ is constant. The scatter noise index is defined as

$$\chi = \int_{\Omega_{\text{det}}} d\Theta\, d\Phi \sin\Theta\, B(\Theta, \Phi) \tag{18}$$

where $\Omega_{\text{det}}$ is the solid angle subtended by the detector in the imaging optics (see, for example, Fig. 11, where the noise source would be at the object plane and the detector, in the CCD plane). Experimentally, $\chi$ can be determined by placing a detector with a collector lens that captures the scatter noise within the solid angle $\Omega_{\text{det}}$. The signal-to-noise ratio is simply

$$\text{SNR}_{\text{sc}} = \frac{\eta}{\chi} \tag{19}$$

where $\eta$ is the page diffraction efficiency of the hologram.

*Interpage Cross-Talk Noise.* We have seen that the angular profile of a page beyond the first minima is small but not negligible. The contributions of many neighboring pages give rise to interpage cross-talk, which can become quite large. Let us start by considering the normalized diffracted signal amplitude for a small modulation [see Eqs. (12) and (10)] near the Bragg condition:

$$S = \text{sinc}\left(\frac{\pi n d \sin(\theta_{\text{R}} + \theta_{\text{S}})}{\lambda \cos\theta_{\text{S}}}\right) \delta\theta_{\text{R}} \tag{20}$$

where $\delta\theta_{\text{R}}$ is the read reference angle detuning. Suppose that a second page is recorded with a reference angle that differs by

$$\Delta\theta_{\text{R}} = \alpha \frac{\lambda \cos\theta_{\text{S}}}{n d \sin(\theta_{\text{R}} + \theta_{\text{S}})} \tag{21}$$

from the page under consideration. For a single wave vector signal beam, the choice of $\alpha = 1, 2, \ldots$ corresponds to zero cross-talk as the peak of the first page coincides with the zero minima of the second, and vice versa. However, if the signal beam has an angular spread $\theta_{\text{S}} \pm \Delta\theta_{\text{S}}$, where $\Delta\theta_{\text{S}} = \tan^{-1}(1/2\sqrt{2}F)$ and $F$ is the *F-number* of the recording optics, the cross-talk is no longer zero. The cross-talk amplitude $X$, which comes from the signal deviation, $-\Delta\theta_{\text{S}} \le \delta\theta_{\text{S}} \le \Delta\theta_{\text{S}}$, is

$$\begin{aligned} X &= \text{sinc}\left[\frac{\pi n d}{\lambda} \frac{\sin(\theta_{\text{R}} + \theta_{\text{S}} + \delta\theta_{\text{S}})}{\cos(\theta_{\text{S}} + \delta\theta_{\text{S}})} \Delta\theta_{\text{R}}\right] \\ &= \text{sinc}[\pi\alpha(1 + \epsilon)] \end{aligned} \tag{22}$$

where

$$\epsilon = [\tan\theta_{\text{S}} + \cot(\theta_{\text{R}} + \theta_{\text{S}})]\delta\theta_{\text{S}} \tag{23}$$

Note that for $\theta_{\text{S}} = 0$ and $\theta_{\text{R}} = 90^\circ$, this linear approximation gives $\varepsilon = 0$ so that we need to examine only the higher-order terms. This is the optimum geometry for maximizing signal-to-noise ratio. This is one of the attractive attributes of the $0^\circ/90^\circ$ geometry (13,31).

The cross-talk as a function of the signal pixel position at three different values of $\alpha$ are shown in Fig. 9, where $\theta_{\text{R}} = \theta_{\text{S}} = 23^\circ$, $n = 1.5$, and $F = 2$.

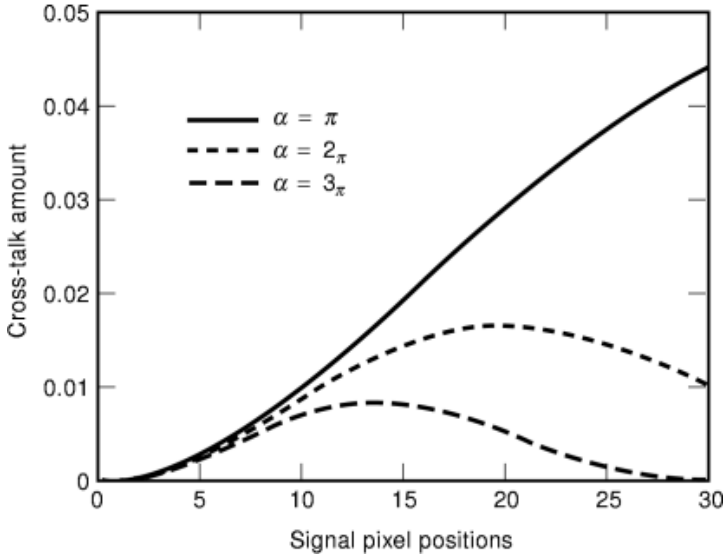


**Fig. 9.** Normalized cross-talk intensity as a function of $\delta\theta_S$ at $\Delta\theta_R = \pi$, $2\pi$, and $3\pi$ for $F = 2$. The pixel position $j = 30$ corresponds to $\delta\theta_S = \Delta\theta_S = 0.24$ rad.

Now we address the problem of cross-talk for complex multiplexed holograms. Suppose that there are $P_L$ pages on the left and $P_R$ pages on the right of a given hologram, then the rms interpage noise-to-signal ratio ($NSR$) is

$$\mathrm{NSR}_{pg} = \sum_{\substack{p=-P_L \\ p\neq 0}}^{P_g} \mathrm{sinc}^2[\pi\alpha p(1+\epsilon)] \tag{24}$$

In most realistic situations, $\varepsilon$ depends only weakly on $\theta_R$, and therefore we treat it as a constant evaluated at the center $\theta_R$. For the first $p_0$ pages where $\pi\alpha p_0\varepsilon$ is small (say up to $\pi/4$), or $p_0 \sim 1/(4\alpha\varepsilon)$, we can use the approximation $\mathrm{sinc}^2[\pi m(1+\varepsilon)] \sim \varepsilon^2$, $m = \alpha p =$ integer. Notice that for small values of $\delta\theta_S$ the approximation is independent of $\alpha$ or $p$, as can be seen in Fig. 9. The noise contribution of the first $p_0$ pages on both sides is

$$2p_0\epsilon^2 = \frac{\epsilon}{2\alpha} \tag{25}$$

For $p \geq p_0$, we use the envelope of the sinc-function to estimate the worst case:

$$2\sum_{p=p_0}^{P_{max}} \left(\frac{1}{\pi\alpha p}\right)^2 = \frac{2}{\pi^2\alpha^2}\sum_{p=p_0}^{P_{max}} \left(\frac{1}{p}\right)^2 \tag{26}$$

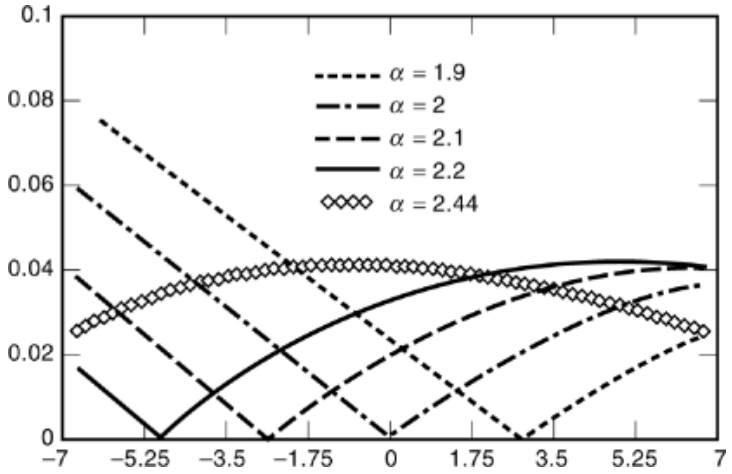


**Fig. 10.** Interpage cross-talk as a function of the pixel positions for a family of $\alpha$ values, where $\alpha$ is a measure of the page angular separation. It is clear from the figure that the optimum choice of $\alpha$ is 2.44 which makes the cross-talk uniform and quite small.

Because $\Sigma^{\infty}_{p=1}\, 1/p^2 = 1.645\ldots$, Eq. (26) will never exceed $0.33/\alpha^2$. Notice that the largest contribution comes from the $p = 1$ term $(0.2/\alpha^2)$. Thus, the total rms interpage cross-talk noise is confined to

$$\mathrm{NSR}_{\mathrm{pg}} \leq \frac{\epsilon}{2\alpha} + \frac{2}{\pi^2\alpha^2}\, s(p_0) \tag{27}$$

Let us estimate the interpage cross-talk for the previous example with $\theta_{\mathrm{R}} = \theta_{\mathrm{S}} = 23^{\circ}$ and $F = 2$. In this case, $\varepsilon = 0.34$. For $\alpha = 2$ ($2\pi$-criteria), $p_0 < 1$, and therefore the first term in Eq. (24) does not contribute. Thus, $\mathrm{NSR}_{\mathrm{pg}} \leq 0.083$ or $\mathrm{SNR}_{\mathrm{pe}} \geq 12$.

Because Eq. (27) gives the worst-case estimate, we provide in Fig. 10 a direct numerical simulation of cross-talk using Eq. (25). At $\alpha = 2$, the cross-talk is zero at the center pixel point but grows rapidly near the edges of the image pattern to 0.06 at the edge of the left side. When the value of $\alpha$ is decreased to 1.9, the zero moves to the right, and the worst-case cross-talk gets larger; but when $\alpha$ is increased, the zero moves in the opposite direction and the worst-case cross-talk value also drops until a more or less uniform cross-talk of less than 0.04 is reached at an $\alpha$ value of 2.44 with this particular example. The best choice of $\alpha$ is actually 2.1, as can be seen from Fig. 10. This slight increase in $\alpha$ results in the lowest-possible interpage cross-talk, and it actually leads to a higher storage density when the density is dynamic range limited, as we will show in more detail in the section entitled "Trade-off Between the Storage Density and the Transfer Rate."

*Detector Noise.* The CCD noise consists of several sources of Johnson thermal noises at the sense node and at the preamps. These noises are lumped together to provide the rms noise electrons $Q_{\mathrm{CCDN}}$. Present technologies can provide $Q_{\mathrm{CCDN}}$ value in the neighborhood of 20 to 50 (32,33). Thus,

$$\mathrm{SNR}_{\mathrm{CCD}} = \frac{\eta P_{\mathrm{R}} \tau_{\mathrm{r}} (\mathrm{QE})}{0.5 N^2_{\mathrm{SLM}} (OS) Q_{\mathrm{CCD}} E_{\lambda}} \tag{28}$$

where $\eta$ is the page diffraction efficiency, $P_{\mathrm{R}}$ the read reference laser power, $\tau_{\mathrm{r}}$ the read time, QE the CCD quantum efficiency, $N^2_{\mathrm{SLM}}$ the number of SLM pixels, $OS$ the CCD-to-SLM oversampling ratio, and $E_{\lambda}$ the

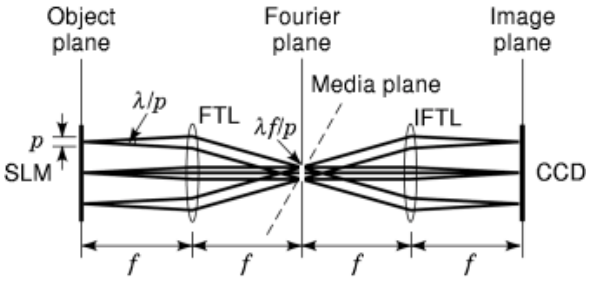


**Fig. 11.** The commonly used geometry of the *f-f-f-f* configuration for Fourier transform recording.

photonic energy at wavelength λ. The factor 0.5 is the result of the 1:1 ratio between the 1s and the 0s in a pseudorandom coded data sequence.

These three noise sources will be utilized to develop the transfer rate in the section entitled "Read Transfer Rate" and also the trade-off between the storage densities and the transfer rates in the section entitled "Trade-off Between the Storage Density and the Transfer Rate." Before that, let us first investigate the storage density using the equations established earlier.

Also for a review of another class of image detectors called CMOS detectors under investigation at many laboratories, see Refs. 34 and 35.

## Storage Density Limits

**Fourier Transform Recording.** Fourier transform recording is a simple method of minimizing the spatial extent of a 2D data pattern. The most common geometry employs an *f-f-f-f* configuration as shown in Fig. 11.

Consider a square spatial light modulator SLM with $N_{\mathrm{SLM}} \times N_{\mathrm{SLM}}$ pixels of pitch $p \times p$ placed at the front focal plane of the Fourier transform lens with *F-number F*. Although the Fourier transform at the back focal plane is extensive, all the fundamental information are contained in the small center portion, a square with side $h$ which equals $\beta$ times the Rayleigh size:

$$h = \beta \frac{\lambda f}{p} = \sqrt{2}\beta\lambda F N_{\mathrm{SLM}} \tag{29}$$

Analysis and empirical tests shows that $\beta$ must be $\geq$1.5 for successful data recovery (6).

Because of the fact that the Fourier transform of a discrete binary pattern is very spotty, local intensities at the transform domain have large fluctuations. This causes a severe burden on the dynamic range of the recording media. The best approach to minimize the impact of this problem is via the use of the random phase shifters proposed in the early 1970s (36,37,38,39,40,41).

**Area per Stack.** The ultimate transverse area used by a hologram stack depends on several other factors: the media thickness, the media refractive index, the reference incident angle, and the signal incident angle. The cross section of a stack is shown in Fig. 12. The incident plane is chosen to lie in the *x–z* plane (see the adopted coordinate system). In this diagram, $\Theta_{\mathrm{R}}$ is the external reference incident angle and $\Theta_{\mathrm{S}}$ is the external signal incident angle. $H_x$ is the linear size of the stack in the $x$ direction and $H_y$, not shown, is the

linear size in the $y$ direction. The angle $\Phi$ is related to the $F$-number of the FTL by

$$\Phi = \tan^{-1}\left(\frac{1}{2\sqrt{2}F}\right) \tag{30}$$

$H_x$ and $H_y$ can be derived using the geometrical diagram of Fig. 12,

$$H_x = g_h(n, F, \Theta_S) \cdot h + g_d(n, F, \Theta_S, \Theta_R) \cdot d \tag{31}$$

and

$$H_y = g_h(n, F, 0) \cdot h + g_d(n, F, 0, 0) \cdot d \tag{32}$$

The multipliers $g_h$ and $g_d$ in Eqs. (31) and (32) are geometrical factors given by

$$g_h(n, F, \Theta_S) = \frac{1}{\cos\Theta_S} + \frac{\tan\Theta_S}{n^2} \times \left[\sqrt{\frac{n^2 - \sin^2\Theta_S}{(8F^2+1)(n^2-\frac{1}{2}) + \frac{1}{2}(8F^2-1)\cos 2\Theta_S - 2\sqrt{2}F\sin 2\Theta_S}} \times (\cos\Theta_S + 2\sqrt{2}F\sin\Theta_S) - \sin\Theta_S\right] \tag{33}$$

$$g_d(n, F, \Theta_S, \Theta_R) = \frac{\cos\Theta_S + 2\sqrt{2}F\sin\Theta_S}{\sqrt{(8F^2+1)(n^2-\frac{1}{2}) + \frac{1}{2}(8F^2-1)\cos 2\Theta_S - 2\sqrt{2}F\sin 2\Theta_S}} + \frac{2\sin\Theta_R}{\sqrt{n^2 - \sin^2\Theta_R}} \tag{34}$$

In angle multiplexing, $\Theta_R$ should be chosen to be the largest reference angle employed. For normal signal incident ($\Theta_S = 0$), Eqs. (33) and (34) simplify to

$$g_h(n, F, 0) = 1 \quad \text{and}$$
$$g_d(n, F, 0, \Theta_R) = \frac{1}{\sqrt{(8F^2+1)n^2 - 1}} + \frac{2\sin\Theta_R}{\sqrt{n^2 - \sin^2\Theta_R}} \tag{35}$$

respectively.

The transverse area of a stack is

$$A = H_x H_y \tag{36}$$

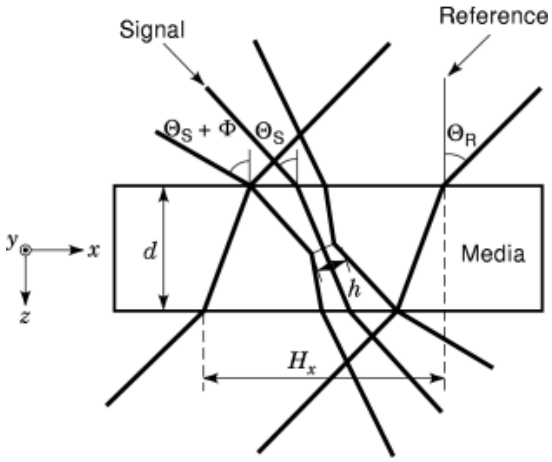


**Fig. 12.** The cross-section of a stack and the optimum placement of the signal beam in the stack.

A useful way to discuss the hologram area is the area per bit for one hologram $A_{\text{bit}}$, which is simply

$$A_{\text{bit}} = \frac{H_x H_y}{N_{\text{SLM}}^2} \tag{37}$$

As an example, $A_{\text{bit}}$ is plotted in Fig. 13 versus the *F-number,* where the media is assumed to have a thickness of 1 mm, and an index of 1.5. Notice that (1) the storage density drops as the number of pixels in the SLM decreases, and (2) an optimum $F_{\text{opt}}$ exists that minimizes the area, and it is dependent on $N_{\text{SLM}}$, $d$, and the recording angles. In the special case where $\Theta_S = 0^\circ$ and under reasonable *F-numbers* (say $F > 1$), $F_{\text{opt}}$ can be well approximated by $\sqrt{d/4\beta\lambda n N_{\text{SLM}}}$. In a numerical example with $\Theta_R = 60^\circ$, $\beta = 1.5$, $\lambda = 0.5$ $\mu$m, $N_{\text{SLM}} = 512$, $n = 2$, $d = 5$ mm suitable for crystal recording, and the value of $F_{\text{opt}}$ becomes as large as 1.3.

**Storage Density.** We have shown the equations for the area occupied per bit for a given hologram in the previous subsection, and if we also know the number of holograms per stack $N_{\text{pg}}$, we will be able to estimate the final density per unit area. We first examine optics limited $N_{\text{pg}}$, denoted by $N_{\text{pgo}}$ resulting from multiplexing, assuming no media limitation, and then examine $N_{\text{pgd}}$ imposed by the limited dynamic range of the recording media. The latter poses a limit for a given material, whereas the former poses the ultimate limit. Equations (16) and (17) provide the formula for $N_{\text{pgo}}$, thus the areal density is

$$D_o = \frac{nd}{\lambda} \cdot \frac{\mu_{\text{MX}}}{\alpha} \cdot \frac{1}{A_{\text{bit}}} \tag{38}$$

where $A_{\text{bit}}$ is area per bit given in Eqs. (31)–(37).

Regarding $N_{\text{pgd}}$, the number depends not only on $\Delta n$ but also on the desired diffraction efficiency $\eta$. Combining Eqs. (8)–(12)and assuming that (1) $\xi^2 + \nu^2 \ll 1$, which is true for memory applications where $\eta$ per page must be small, and (2) each page consumes the same amount of $\delta n$, that is $\Delta n = N_{\text{pgd}}\delta n$, we obtain

$$N_{\text{pgd}} = \frac{\pi d \Delta n}{\lambda \sqrt{\eta} \sqrt{c_S c_R}} \tag{39}$$

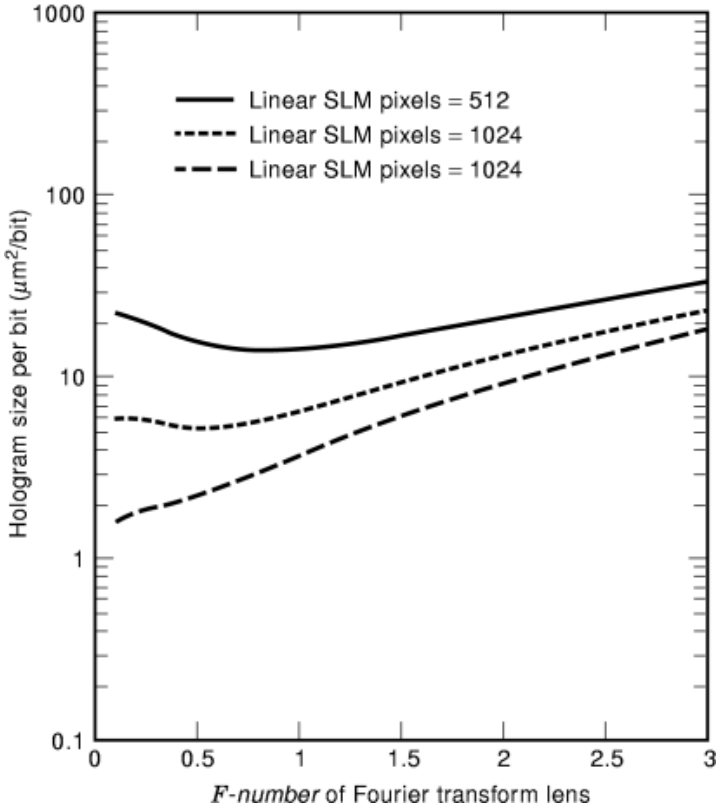


**Fig. 13.** Area per bit per hologram versus the *F-number* using the optimum recording geometry shown in Figure 12. In this example, $d = 1$ mm, $\lambda = 500$ nm, $\Theta_R = \Theta_S = 35^\circ$.

thus

$$D_d = \frac{\pi d \Delta n}{\lambda \sqrt{\eta e^{ad}} \sqrt{c_S c_R}} \cdot \frac{1}{A_{bit}} \tag{40}$$

In the following figures, we show the storage density potential for both the photopolymers (42,43,44,45,46,47, 48,49,50,51) and the photorefractive signel crystals (52,53,54) such as $LiNbO_3$. The former has an index about 1.5 and may potentially have a relatively large $\Delta n$ of $10^{-3}$ to $10^{-2}$. However, its thickness is not likely to become scalable to more than 1 mm because of dye absorption and the relatively large media noise in photopolymers. The latter has an index near 2.3 and a small $\Delta n$ of $10^{-5}$ to $10^{-4}$, but low absorption and low noise for crystals unburdened with striation problems.

Figure 14 shows the storage density, expressed in bits per square inch, versus the available $\Delta n$ of the first class of materials for a family of required $\eta$. The medium thickness is taken to be 1 mm and the absorption $e^{-ad} = 0.3$, an FT lens with $F = 2$, $\Theta_R = \Theta_S = 35^\circ$, and there is a reference beam swing angle of $\pm 35^\circ$ at the medium plane. The interpage separation factor $\alpha$ is set at 2.1 (see the subsection entitled "Interpage Cross-talk Noise" and Fig. 10 for the rationale behind this choice). The SLM has 512 $\times$ 512 pixels. The solid horizontal line is the density limits set by optics (i.e., Bragg selectivity). One sees from this particular example that the storage

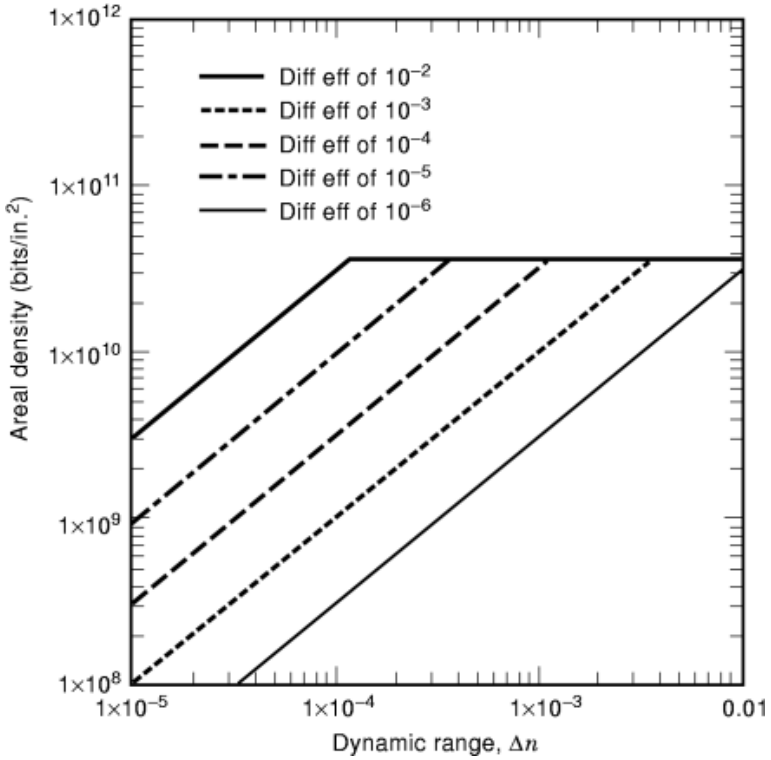


**Fig. 14.** Equivalent area density versus the media dynamic range for a photo-polymer like material. The optics-limited density is the solid horizontal line at the top. $d = 1$ mm, $\lambda = 500$ nm, $F = 2$, $n = 1.5$.

density ceiling is $3.5 \times 10^{11}$ bits/in.$^2$. Even at a high $\eta$ of $10^{-2}$ per page, the limit can be reached if the material has a $\Delta n$ of slightly more than $10^{-2}$.

Figure 15 shows the storage density for the second class of materials where we have assumed a medium thickness of 3 mm and FT lens with $F = 2$ speed, not very far from the optimum *F-number,* as pointed out in the subsection entitled "Area Per Stack." Other parameters are the same as those used in Fig. 14. One sees that the storage density ceiling imposed by optics is only slightly higher at $4.5 \cdot 10^{11}$/in.$^2$, even though the medium thickness has increased three-fold. However, because of the smaller available $\Delta n$ of about $10^{-4}$ of most known crystals, it is not easy to reach the optics limit unless very low $\eta$ can be tolerated. That implies that very low medium noise is needed. More on the subject of the dependence of density on noise will be discussed in the section entitled "Trade-off Between the Storage Density and the Transfer Rate."

Another important point to be made is that the curves in Figs. 14 and 15 are not much different. This is simply the result of the fact that when one records a hologram from the same side of the material, the useful $\boldsymbol{k}$ space is about the same if the external angles are the same. In this case, both simulations are done at $\Theta_R$ and $\Theta_S$ of 35°, and there is a reference beam swing angle of ±35° at the medium plane. The reason that a medium thickness of 1 mm versus 3 mm has not made much difference is discussed next.

Because the hologram size increases very quickly with medium thickness, we suspect that there might be an optimum thickness beyond which the storage density will start to decrease. The example shown in Fig. 16 is for a material of $\Delta n$ of $10^{-4}$ and $F = 2$, which is suitable for a material like $LiNbO_3$. Here density versus thickness is plotted for a family of $\eta$ per page. Again the solid curve at the top is the optics-imposed storage limit, where we see an optimum at 3 mm. Because the optimum is at a relatively broad peak, a media thickness

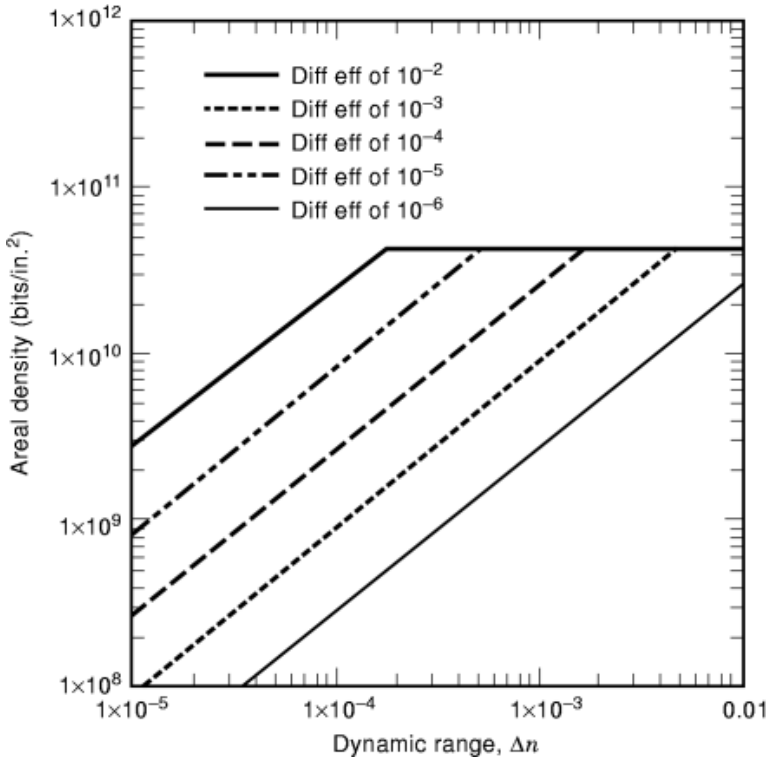


**Fig. 15.** Equivalent area density versus the media dynamic range for a $LiNbO_3$ like material. The optics-limited density is the solid horizontal line at the top. $d = 3$ mm, $\lambda = 500$ nm, $F = 2$, $n = 2.3$.

of 1 to 2 mm is sufficient for density maximization. Furthermore, if the diffraction efficiency per page is larger than $10^{-6}$, then the density will always be $\Delta n$ limited and the density maximum occurs at about 1.5 mm.

## Read Transfer Rate

Generally, signal recovery for high-density signals requires a broadband SNR of at least 14 dB or 5:1. Because the noise in a broadband signal is linearly proportional to the channel bandwidth, higher transfer rates mean higher noises, and therefore a larger signal level is required, or a larger $\eta$ is needed. Even though the amount of media noise and the interpage cross-talk noise discussed previously are linearly proportional to $\eta$, the CCD noise is not. Our approach is to sum all the noise contributors formulated in the subsection entitled "Noise" from which we derive the relationship between the transfer rate and the various noise parameters and the diffraction efficiency.

First of all, from Eq. (28), the CCD SNR is given by

$$\mathrm{SNR}_{\mathrm{CCD}} = \frac{\eta P_{\mathrm{R}} \tau_{\mathrm{read}} (\mathrm{QE})}{0.5 N_{\mathrm{SLM}}^2 (\mathrm{OS}) Q_{\mathrm{CCD}} E_\lambda} = \frac{\eta \cdot b P_{\mathrm{R}}}{Q_{\mathrm{CCDN}} \cdot \nu_{\mathrm{read}}} \qquad (41)$$

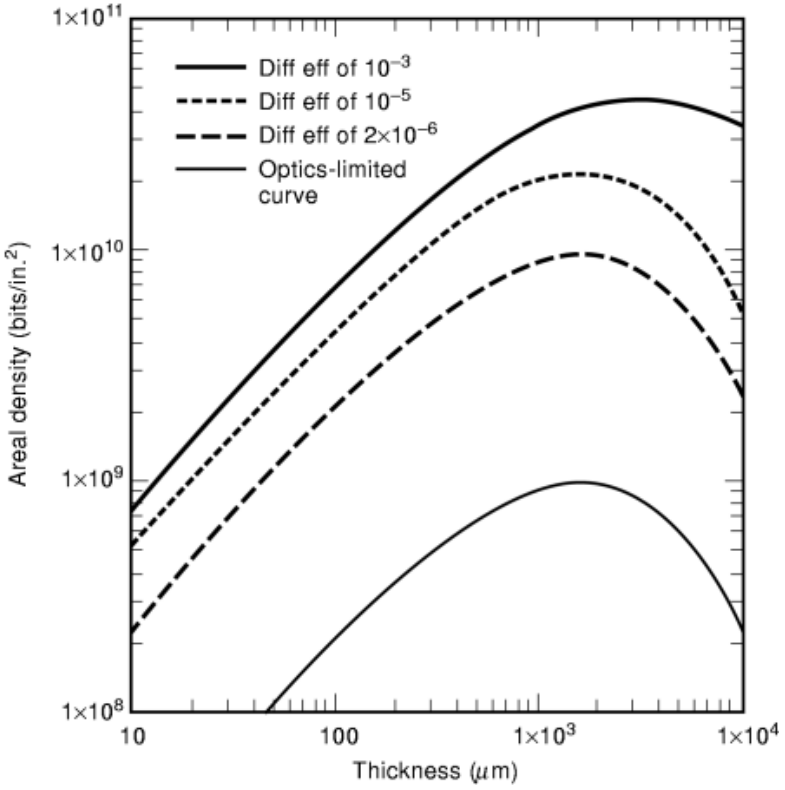


**Fig. 16.** Equivalent area density versus thickness at various diffraction efficiencies, where $\lambda = 500$ nm, $F = 2$, $n = 2.3$, $\Delta n = 10^{-4}$. Notice the optimum near a thickness of 2 mm in this case.

where

$$b = \frac{2QE}{p \cdot \mathrm{OS} \cdot E_\lambda} \tag{42}$$

$\nu_{\mathrm{read}}$ is the effective data transfer rate, that is,

$$\nu_{\mathrm{read}} = \frac{N_{\mathrm{bit}}}{T_{\mathrm{xfr}} + T_{\mathrm{read}}} \tag{43}$$

and

$$p = \frac{T_{\mathrm{xfr}} + T_{\mathrm{read}}}{T_{\mathrm{R}}} \tag{44}$$

where $T_{\mathrm{read}}$ is the CCD exposure time and $T_{\mathrm{xfr}}$ is the actual CCD frame transfer time.

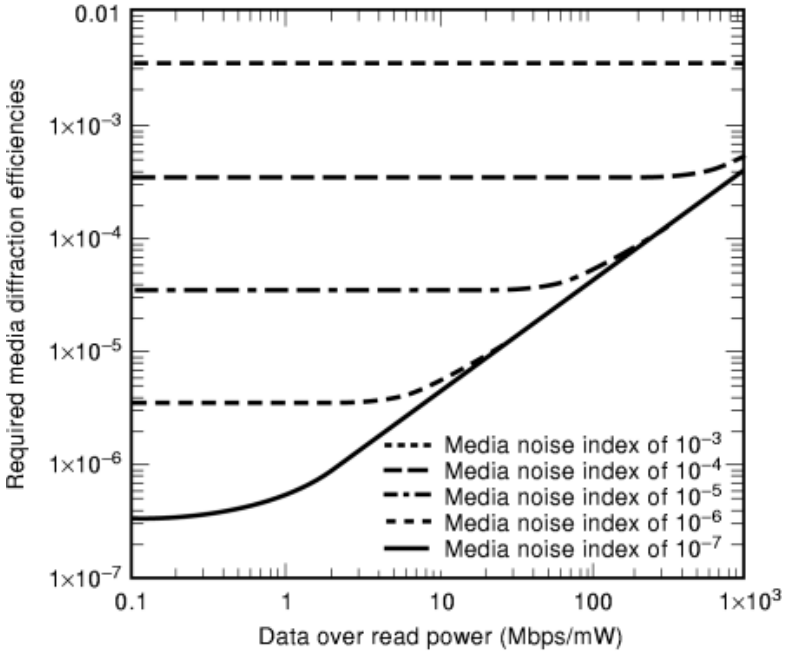


**Fig. 17.** Required diffraction efficiencies versus data rate per unit read power, for a family of media noise indices.

The media signal-to-noise, as defined in Eq. (19), is

$$\mathrm{SNR}_{\mathrm{sc}} = \frac{\eta}{\chi}$$

Thus the required $\mathrm{SNR}^{-1}$, or NSR, of the detection system is related to the media noise, the interpage cross-talk, and the CCD noise electrons by

$$\mathrm{NSR}^2 = \frac{\chi^2}{\eta^2} + \mathrm{NSR}_{\mathrm{pg}}^2 + \frac{Q_{\mathrm{CCDN}}^2 \nu_{\mathrm{read}}^2}{b^2 \eta^2 P_{\mathrm{R}}^2} \tag{45}$$

Thus, the required $\eta$ to support the desired $\nu_{\mathrm{read}}/P_{\mathrm{R}}$ is

$$\eta^2 = \frac{\chi^2 + Q_{\mathrm{CCDN}}^2 \nu_{\mathrm{read}}^2 / b^2 P_{\mathrm{R}}^2}{\mathrm{NSR}^2 - \mathrm{NSR}_{\mathrm{pg}}^2} \tag{46}$$

We plot the $\eta$ dependence on $\nu_{\mathrm{read}}/P_{\mathrm{R}}$ in Fig. 17 for a family of media noise indices. We have assumed $Q_{\mathrm{CCDN}} = 50$, $\mathrm{NSR} = 0.1$ and $\mathrm{NSR}_{\mathrm{pg}} = 0.04$ (see the subsection entitled "Interpage Cross-talk Noise") in this example. Also, the following values are chosen: $\mathrm{QE} = 0.5$, $E_\lambda = 2\mathrm{ev}$, $N_{\mathrm{SLM}} = 512$, $\mathrm{OS} = 4$, and $p = 2$.

Several observations can be drawn from Fig. 17:

(1) As we start at a low value of $\nu_{\mathrm{read}}/P_{\mathrm{R}}$, the first term related to media noise in the numerator of Eq. (46) is much larger than the second term, which is tied with the CCD noise, and $\eta$ is essentially independent of

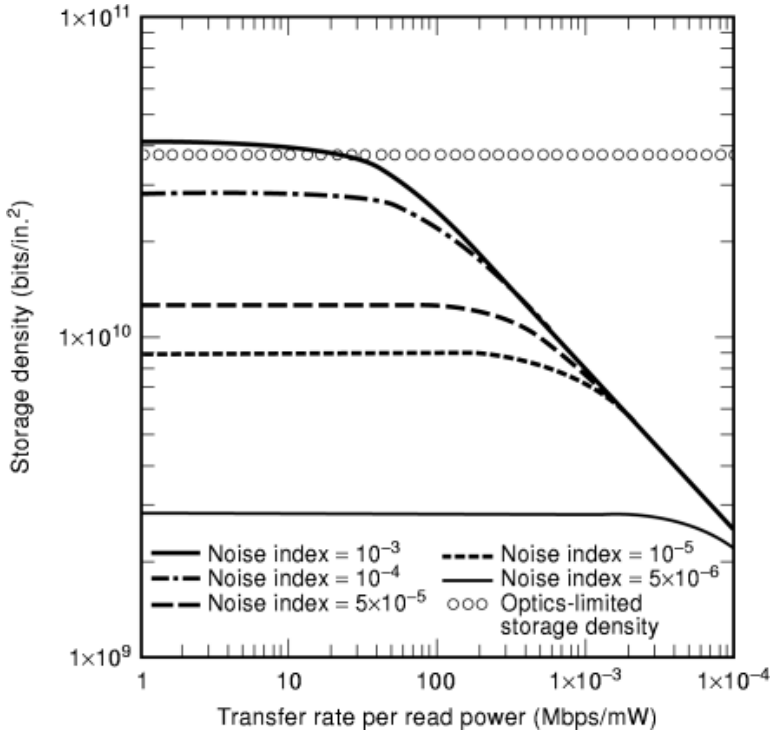


**Fig. 18.** Trade-off of storage density versus data rate per unit read power, where $d = 1$ mm, $\Delta n = 10^{-3}$, $\lambda = 500$ nm, $\text{NSR}_{\text{pg}} = 0.04$, $\text{NSR} = 0.1$, $F = 2$, $\alpha = 2.1$, $\Theta_{\text{R}} = \Theta_{\text{S}} = 35^{\circ}$.

$\nu_{\text{read}}/P_{\text{R}}$. Then the CCD noise starts to become competitive with the media noise leading to higher values of $\eta$ as $\nu_{\text{read}}/P_{\text{R}}$ increases. Finally, all curves merge into the slanted linear asymptote, which is controlled by the CCD noise floor, where the media noise and the interpage cross-talk become negligible to the noise bandwidth product of the CCD.

(2) For photorefractive crystals like $LiNbO_3$ where the media noise is low, we can support a modest $\nu_{\text{read}}/P_{\text{R}}$ with very low $\eta$, thus making possible very large storage densities. However, if an aggressive transfer rate is desired, then $\eta$ must be made larger, causing reduced storage density. The opposite is true for the photopolymers where the media noise is relatively large, thus higher diffraction efficiencies are needed independent of $\nu_{\text{read}}/P_{\text{R}}$ until a much larger value of $\nu_{\text{read}}/P_{\text{R}}$ is reached. But utilization of the available $\Delta n$ is not as effective, causing penalties in storage density. We will devote the next section to a more quantified discussion of this point.

## Trade-Off Between The Storage Density and The Transfer Rate

The storage density $D$ under dynamic-range-limited situation is given by, from Eq. (40),

$$D_d = \frac{K_1}{\sqrt{\eta}} \tag{47}$$

where

$$K_1 = \frac{\pi \cdot d\,\Delta n}{\lambda\sqrt{e^{ad} c_S c_R}} \cdot \frac{1}{A_{bit}} \tag{47a}$$

where $A_{bit}$ is the area per bit for a single hologram with $N^2_{SLM}$ bits, defined in Eq. (36). Also the required $\eta$ to support the desired $\nu_{read}/P_R$ is, from Eq. (46),

$$\eta^2 = \frac{\chi^2 + Q^2_{CCDN}\nu^2_{read}/b^2P^2_R}{NSR^2 - NSR^2_{pg}} \tag{46}$$

Combining Eqs. (46) and (47) yields

$$D_d = K_2[NSR^2 - NSR^2_{pg}]^{1/4} \tag{48}$$

where

$$K_2 = \frac{K_1}{\left[\mu^2_M + \dfrac{Q^2_{CCDN}}{b^2}\dfrac{\nu^2_R}{P^2_R}\right]^{1/4}} \tag{48a}$$

or

$$D_d\left[\chi^2 + \frac{Q^2_{CCDN}}{b^2}\left(\frac{\nu^2_{read}}{P^2_R}\right)^2\right]^{1/4} = \frac{\pi \cdot d\,\Delta n}{\lambda\sqrt{c_S c_R e^{ad}} A_{bit}}[NSR^2 - NSR^2_{pg}]^{1/4} \tag{49}$$

Equation (49) describes the trade-off between storage density and the read data rate under the $\Delta n$ limited situation. At a relatively modest data rate,

$$\chi^2 \gg \frac{Q^2_{CCDN}}{b^2}\left(\frac{\nu^2_{read}}{P^2_R}\right) \tag{50}$$

and Eq. (49) is approximated by

$$D_d \cong \frac{\pi \cdot d\,\Delta n}{\lambda\sqrt{c_S c_R e^{ad}}\sqrt{\chi}}\frac{1}{A_{bit}}[NSR^2 - NSR^2_{pg}]^{1/4} \tag{51}$$

Equation (51) teaches that $D_d$ will be constant first and then fall off when Eq. (50) no longer holds. See Fig. 18. Also, it is quite clear from Eqs. (49) and (51) that the larger $SNR_{pg}$ is with respect to SNR and the smaller the media noise index is, the higher the storage density will be. Using Eq. (49) we plot the storage density $D$ against $\nu_{read}/P_R$ in Fig. 18. The family of curves has a constant $\Delta n$ of $10^{-3}$, but different values of

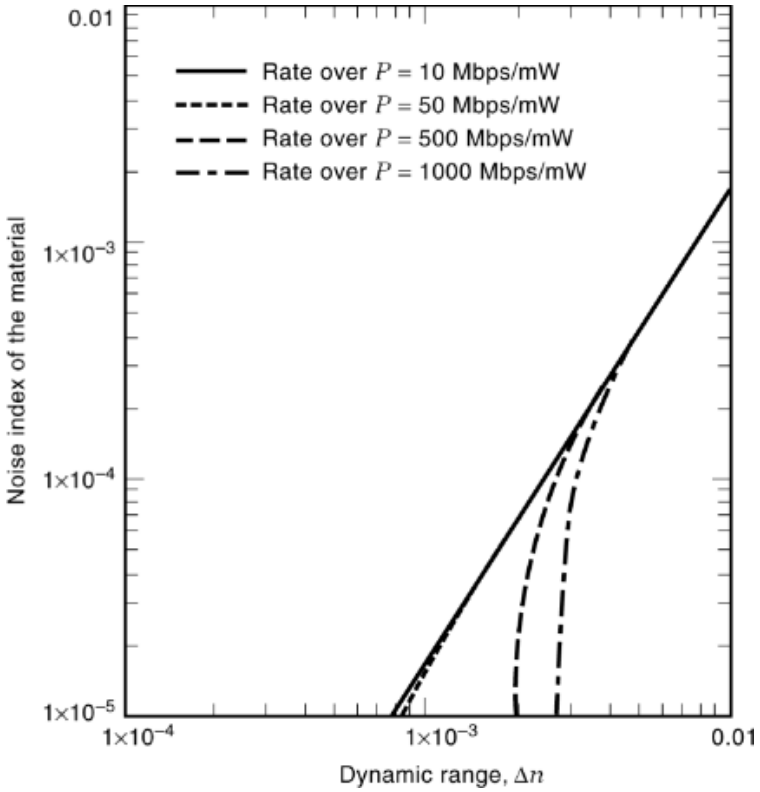


**Fig. 19.** Trade-off of noise index $\chi$ versus dynamic range $\Delta n$ in order to reach optics-limited density, for a family of transfer rates. $\mathrm{NSR_{pg}} = 0.04$, $\mathrm{NSR} = 0.1$.

media noise indices. Again the value of $\alpha$ is chosen to be 2.1, giving $\mathrm{SNR_{pg}}$ a value of 25, see the subsection entitled "Interpage Cross-talk Noise" and Fig. 10. One notices the trade-off of density versus the data transfer rate and also the importance of minimizing the media noise $\chi$ to achieve a large storage density.

As stated earlier, when the storage density is driven to the optics limit, then it becomes, see the subsection entitled "Storage Density,"

$$D_\circ = \frac{nd}{\lambda} \cdot \frac{\mu_{\mathrm{MX}}}{\alpha} \cdot \frac{1}{A_{\mathrm{bit}}} \tag{38}$$

Equating Eqs. (38) and (48) yields

$$\left[\chi^2 + \frac{Q^2_{\mathrm{CCDN}}}{a^2}\left(\frac{\nu_{\mathrm{R}}^2}{P_{\mathrm{R}}^2}\right)^2\right]^{1/2} = \left[\frac{\pi \cdot \alpha \cdot \Delta n}{\xi_{\mathrm{G}} n \sqrt{c_{\mathrm{S}} c_{\mathrm{R}} e^{ad}}}\right]^2 [\mathrm{NSR}^2 - \mathrm{NSR}_{\mathrm{pg}}^2]^{1/2} \tag{52}$$

Equation (52) provides the relationship among all the material parameters when the optics limit is reached. Note that there is no optics dependence (beam angles, *F-number,* etc.) nor is there any significant dependence on medium thickness except for the absorption term, $e^{ad}$.

Because it might be easier to develop media with a smaller media noise index than a larger $\Delta n$, we show in Fig. 19 the trade-off of $\chi$ versus $\Delta n$ under an optics-limited situation. Several characteristics stand out clearly: (1) the required $\Delta n$ to reach optics-limited performance is about $10^{-3}$ to $10^{-2}$ depending on the desired transfer rate (this we believe is an achievable goal for photopolymers); (2) we can make up the lack of a large $\Delta n$ by means of lower noise index to reach the optics-limited capacity; and (3) relatively larger values of $\Delta n$ are needed for larger transfer rates, no matter how small the noise index is.

## BIBLIOGRAPHY


1. J. F. Heanue M. C. Bashaw L. Hesselink Volume holographic storage and retrieval of digital data, *Science*, **295**: 749–752, 1994.
2. J. H. Hong *et al.* Volume holographic memory systems: Techniques and architectures, *Opt. Eng.*, **34**: 2193–2203, 1995.
3. D. Psaltis F. Mok Holographic memories, *Sci. Amer.*, **273** (5): 52–58, 1995.
4. M.-P. Bernal *et al.* A precision tester for studies of holographic optical storage materials and recording physics, *Appl. Opt.*, **35**: 2360–2374, 1996.
5. I. McMichael *et al.* Compact holographic storage demonstrator with rapid access, *Appl. Opt.*, **35**: 2375–2379, 1996.
6. T. C. Lee *et al.* Holographic optical data storage for desktop computer, *Proc. SPIE*, **2514**: 340–354, 1995.
7. P. J. van Heerden Theory of information storage in solids, *Appl. Opt.*, **2**: 393–400, 1963.
8. E. N. Leith *et al.* Holographic data storage in three-dimensional media, *Appl. Opt.*, **5**: 1303–1311, 1966.
9. J. A. Rajchman Holographic optical memory: an optical read-write memory, *Appl. Opt.*, **9**: 2269–2271, 1970.
10. E. G. Ramberg Holographic information storage, *RCA Rev.*, **33**: 5–53, 1972.
11. B. Hill Some aspects of a large capacity holographic memory, *Appl. Opt.*, **11**: 182–191, 1972.
12. G. R. Knight Holographic memories, *Opt. Eng.*, **14**: 453–459, 1975.
13. C. Gu *et al.* Cross-talk-limited storage capacity of volume holographic memory, *J. Opt. Soc. Amer.*, **A9**: 1978–1983, 1992.
14. H. Kogelnik Coupled wave theory for thick hologram gratings, *Bell Sys. Tech. J.*, **18**: 2909–2947, 1969.
15. F. H. Mok *et al.* Storage of 500 high-resolution holograms in $LiNbO_3$ crystal, *Opt. Lett.*, **16**: 605–607, 1991.
16. F. H. Mok Angle-multiplexed storage of 5000 holograms in lithium niobate, *Opt. Lett.*, **18**: 915–917, 1993.
17. X. An D. Psaltis Experimental characterization of an angle-multiplexed holographic memory, *Opt. Lett.*, **20**: 1913–1915, 1995.
18. G. A. Rakuljic V. Leyva A. Yariv Optical data storage by using orthogonal wavelength-multiplexed volume holograms, *Opt. Lett.*, **17**: 1471–1473, 1992.
19. A. Pu *et al.* Storage density of peristhropic multiplexing, *OSA Annu. Meet.*, Dallas, TX, 1994.
20. K. Curtis A. Pu D. Psaltis Method for holographic storage using peristrophic multiplexing, *Opt. Lett.*, **19**: 993–994, 1994.
21. D. Psaltis *et al.* Holographic storage using shift multiplexing, *Opt. Lett.*, **20**: 782–784, 1995.
22. G. Barbastathis *et al.* Holographic 3D disks using shift multiplexing, *Proc. SPIE*, **2514**: 1995, pp. 355–362.
23. G. Barbastathis M. Levene D. Psaltis Shift multiplexing with spherical reference waves, *Appl. Opt.*, **35**: 2403–2417, 1996.
24. V. N. Morozov Theory of holograms formed using a coded reference beam, *Sov. J. Quantum. Electron.*, **7**: 961–964, 1977.
25. A. A. Vasil'ev S. P. Kotova V. N. Morozov Pseudorandom signals as key words in an associative holographic memory, *Sov. J. Quantum. Electron.*, **9**: 1440–1441, 1979.
26. C. Denz *et al.* Volume hologram multiplexing using deterministic phase encoding method, *Opt. Commun.*, **85**: 171–176, 1991.
27. Y. Taketomi *et al.* Incremental recording for photorefractive hologram multiplexing, *Opt. Lett.*, **16**: 1774–1776, 1991.
28. J. Trisnadi S. Redfield Practical verification of hologram multiplexing without beam movement, *Proc. SPIE*, **1773**: 1992, pp. 362–371.

29. G. Denz *et al.* Potentialities and limitations of hologram multiplexing by using the phase-encoding technique, *Appl. Opt.*, **31**: 5700–5775, 1992.
30. C. Alves G. Pauliat G. Rosen Dynamic phase-encoding storage of 64 images in $BaTiO_3$ photorefractive crystal, *Opt. Lett.*, **19**: 1894–1896, 1994.
31. M. C. Bashaw *et al.* Cross-talk considerations for angular and phase-encoded multiplexing in volume holography, *J. Opt. Soc. Amer.*, **B11**: 1820–1836, 1994.
32. W. Lawler *et al.* Performance of high frame rate, back illuminated CCD imagers, *SPIE*, **2172**: 1994, pp. 90–99.
33. P. A. Levine *et al.* Multi-pot backside illuminated CCD imagers for moderate to high frame rate camera applications, *SPIE*, **2172**: 1994, pp. 100–114.
34. E. R. Fossum Active pixel sensors: Are CCD dinosaurs?, *SPIE*, **1900**: 1993, pp. 2–14.
35. S. K. Mendis *et al.* Progress in CMOS active pixel image sensor, *SPIE*, **2172**: 1994, pp. 19–29.
36. C. B. Burckhardt Use of random phase mask for the recording of Fourier transform holograms of data masks, *Appl. Opt.*, **9**: 695–700, 1970.
37. Y. Takeda Holographic memory with high quality and high information storage density, *J. Appl. Phys.*, **11**: 656–665, 1972.
38. Y. Takeda Y. Oshida Y. Miyamura Random phase shifters for Fourier transformed holograms, *Appl. Opt.*, **11**: 818–822, 1972.
39. W. C. Stewart A. H. Firester E. C. Fox Random phase data masks: Fabrication tolerances and advantages of four phase level masks, *Appl. Opt.*, **11**: 604–608, 1972.
40. W. J. Dallas Deterministic diffusers for holography, *Appl. Opt.*, **12**: 1179–1187, 1973.
41. Y. Nakayama M. Kato Linear recording of Fourier transform holograms using a pseudorandom diffuser, *Appl. Opt.*, **21**: 1410–1418, 1982.
42. D. H. Close *et al.* Hologram recording on photopolymer materials, *Appl. Phys. Lett.*, **14**: 159–160, 1969.
43. W. S. Colburn K. A. Haines Volume hologram formation in photopolymer materials, *Appl. Opt.*, **10**: 1636–1641, 1971.
44. R. H. Wopschall T. R. Pampalone Dry photopolymer film for recording holograms, *Appl. Opt.*, **11**: 2096–2097, 1972.
45. B. L. Booth Photopolymer material for holography, *Appl. Opt.*, **11**: 2994–2995, 1972.
46. B. L. Booth Photopolymer material for holography, *Appl. Opt.*, **14**: 593–601, 1975.
47. A. M. Weber *et al.* Hologram recording in DuPont's new photopolymer materials in Practical Holography IV, *Proc. SPIE*, **1212**: 1990, pp. 30–39.
48. W. J. Gambogi A. M. Weber T. J. Trout Advances and applications of DuPont holographic photopolymers in Holographic Imaging and Materials, *Proc. SPIE*, **2043**: 1993, pp. 2–13.
49. R. T. Ingwall H. L. Fielding Hologram recording with a new Polaroid photopolymer system in applications of holography, *Proc. SPIE*, **523**: 1985, pp. 306–312.
50. R. T. Ingwall M. Troll Mechanism of hologram formation in DMP-128 photopolymer, *Opt. Eng.*, **28**: 586–591, 1989.
51. D. A. Waldman *et al.* Cationic Ring-opening photopolymerization methods for volume hologram recording in diffractive and holographic optics technology III, *Proc. SPIE*, **2689**: 1996, pp. 127–141.
52. P. Gunter J.-P. Huignard *Photorefractive Materials and Their Applications*, Vols. I and II, Berlin: Springer Verlag, 1988 and references therein.
53. Special issues on photorefractive crystals, *J. Opt. Soc. Amer. B:* August 1988, August 1992, September 1994 and references therein.
54. P. Yeh *Introduction to Photorefractive Nonlinear Optics*, New York: Wiley, 1993.

TZUO-CHANG LEE
Eastman Kodak Company
JAHJA TRISNADI
Silicon Lights Machines